JOURNAL OF SPACECRAFT AND ROCKETS
Vol. 47, No. 6, November–December 2010

Boundary-Layer Transition on X-43A

Scott Berry,* Kamran Daryabeigi,† and Kathryn Wurster‡
NASA Langley Research Center, Hampton, Virginia 23681
and
Robert Bittner§
ATK Space Division, Hampton, Virginia 23681

DOI: 10.2514/1.45889

The successful Mach 7 and 10 flights of the first fully integrated scramjet propulsion systems by the Hyper-X (X-43A) program have provided the means with which to verify the original design methodologies and assumptions. As part of Hyper-X's propulsion-airframe integration, the forebody was designed to include a spanwise array of vortex generators to promote boundary-layer transition ahead of the engine. Turbulence at the inlet is thought to provide the most reliable engine design and allows direct scaling of flight results to ground-based data. Preflight estimations of boundary-layer transition, for both Mach 7 and 10 flight conditions, suggested that forebody boundary-layer trips were required to ensure fully turbulent conditions upstream of the inlet. This paper presents the results of an analysis of the thermocouple measurements used to infer the dynamics of the transition process during the trajectories for both flights, on both the lower surface (to assess trip performance) and the upper surface (to assess natural transition). The approach used in the analysis of the thermocouple data is outlined, along with a discussion of the calculated local flow properties that correspond to the transition events as identified in the flight data. The present analysis has confirmed that the boundary-layer trips performed as expected for both flights, providing turbulent flow ahead of the inlet during critical portions of the trajectory, while the upper surface was laminar as predicted by the preflight analysis.

Nomenclature

k	=	trip height, in.
M_e	=	edge Mach number
P_∞	=	freestream pressure, lb./ft^2
R_n	=	nose radius, in.
Re_θ	=	momentum thickness Reynolds number
T	=	surface temperature, deg-R
T_∞	=	freestream temperature, deg-R
t	=	time from B-52 drop, s
δ	=	boundary-layer thickness, in.
α	=	angle of attack, deg

I. Introduction

NASA'S Hyper-X (X-43A) program has successfully flown an airframe-integrated scramjet propulsion system at hypersonic conditions. Two flights were achieved to Mach 7 and Mach 10. An overview of the preflight wind-tunnel test program can be found in [1–3], and flight results have recently been published in [4–6]. An artist's rendition of the X-43A vehicle in flight during the scramjet propulsion experiment is provided in Fig. 1a, while Fig. 1b provides a photograph during the boost stage for the first flight to Mach 7. This program has provided the first opportunity to obtain flight data on an autonomous hypersonic air-breathing propulsion system that is fully integrated with the vehicle airframe, and will validate/calibrate the experimental, numerical, and analytical methods that were used for design and flight performance prediction. To reduce uncertainties associated with this cutting-edge technology maturation program before flight, a systematic and combined experimental and numerical approach was used. Technological advancements, required before flight, included development of aerodynamic performance and aeroheating databases, verification of performance and operability of the propulsion-airframe integration, and establishment of a method for boundary-layer control. The present paper focuses on the development and use of boundary-layer trips required as part of the engine inlet flow path. To provide the most robust scramjet propulsion system, the boundary layer approaching the scramjet inlet should be turbulent. Ingestion of a turbulent boundary layer increases inlet operability (by reducing susceptibility to flow separations within the engine) and therefore enhances overall engine performance. During the nominal flight condition, the location of natural transition on the Hyper-X forebody was estimated to be far downstream of the inlet station based on best estimates of boundary-layer transition for slender, planar configurations at hypersonic flight conditions (to be discussed in more detail). Thus, boundary-layer trip devices were deemed necessary to ensure a turbulent boundary layer at the inlet for both Mach 7 and 10 flights. To develop boundary-layer trips for the Hyper-X vehicle, a wind-tunnel test program was initiated at the NASA Langley Research Center (LaRC), which is detailed in [7]. It is important to note that the Hyper-X flight-test program was first and foremost a scramjet experiment and that obtaining boundary-layer transition data was only one of many secondary objectives. Nevertheless, these successful flights provide an excellent opportunity to use the in-flight measurements to verify the many methods and assumptions used to design the vehicle. In this regard, the goal of the present paper is to present an analysis of the Hyper-X flight boundary-layer transition data, both in terms of the trip design and the natural transition measurements from the upper surface.

A. Hypersonic Boundary-Layer Transition

As part of the fully integrated scramjet propulsion system, the lower surface forebody of the Hyper-X vehicle was designed to compress and process the flow going into the inlet. The forebody, see Fig. 2, is approximately 6-ft long and is characterized by a thin

Presented as Paper 3736-2008 at the 38th Fluid Dynamics Conference and Exhibit, Seattle, WA, 23–26 June 2008; received 8 June 2009; revision received 27 August 2010; accepted for publication 16 September 2010.

*Aerospace Engineer, Aerothermodynamics Branch, M/S 408A. Associate Fellow AIAA.
†Aerospace Engineer, Structural Mechanics and Concepts Branch, M/S 190. Senior Member AIAA.
‡Aerospace Engineer, Vehicle Analysis Branch, M/S 451. Associate Fellow AIAA.
§Aerospace Engineer, Hypersonic Air Breathing Propulsion Branch, M/S 168.

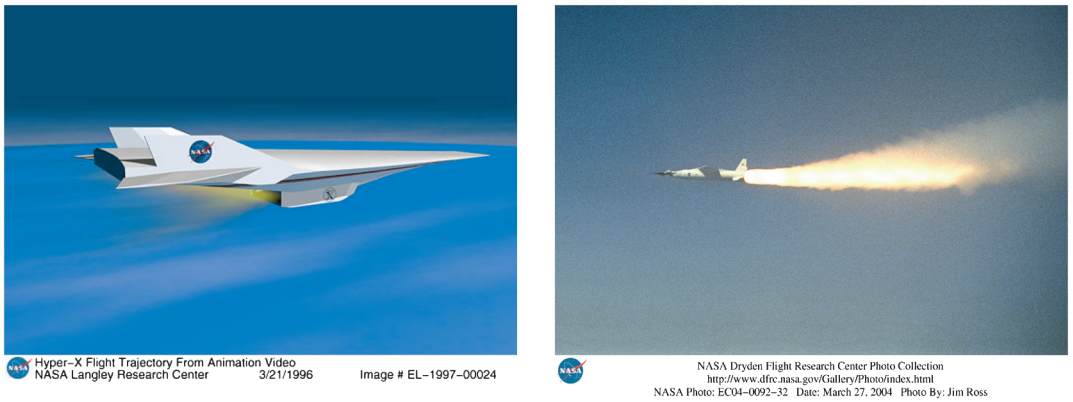

a) b)

Fig. 1 Illustrations of a) scramjet powered flight of Hyper-X, and b) Pegasus boost of Hyper-X vehicle to Mach 7.

leading edge ($R_n = 0.03$-in for the Mach 7 vehicle, 0.05-in. for Mach 10) and three flat ramps on the lower surface that provide a series of discrete, nonisentropic flow-compressions for the engine. At the nominal angle of attack of 2-deg (original design point for the Mach 7 vehicle, later changed to 2.5 deg), the first ramp provides an initial 4.5 deg of compression, followed by an additional 5.5 deg on the second ramp, and a final 3 deg of compression on the third ramp. Outboard of the flat ramps are the chines, which are designed to minimize three-dimensional effects and flow spillage. Ideally, the forebody would also provide a turbulent boundary layer for the inlet. A full-scale scramjet-powered vehicle, such as the National Aerospace Plane (NASP) or a similar derivative, would likely have sufficient forebody length to provide a naturally turbulent boundary layer. Hyper-X is subscale to a NASP-like vehicle and thus requires forced boundary-layer transition to properly scale these engine flight-test results to a future full-scale vehicle, as well as to ground-based data. While the primary emphasis is for the trips to provide turbulence for the inlet, a secondary goal is to alleviate the likelihood of a laminar separation at the first ramp corner. Flow separation at the first corner has the potential to promote lateral spillage of the boundary layer away from the inlet, thus reducing mass capture and affecting engine performance.

An assessment of the Hyper-X forebody using the hypersonic boundary-layer transition criteria developed during the NASP program [8] suggested that the vehicle forebody would be laminar at the nominal test condition [9]. Laminar values of the momentum thickness Reynolds number over edge Mach number (Re_θ/M_e) for a sharp-nose wedge with 4.5 deg of compression were computed. The NASP sharp planar transition criterion of $Re_\theta/M_e = 305$ was used to estimate the onset of transition. For an initial assessment, this sharp planar criterion was deemed acceptable, as nose bluntness has a stabilizing influence that would further delay transition onset [10]. Based on this initial estimate for a smooth configuration, transition would not occur on the first ramp before the compression corner. In fact, over 200% more running length is required for transition to occur on the first ramp based on the NASP criterion, which is beyond the inlet. Thus, without a boundary layer trip, the potential exists for a laminar separation at the first ramp break that could generate some degree of lateral flow spillage. As for the question of transition before the inlet, a discrete compression corner is likely to promote transition (through instabilities within the separation/reattachment process), but to what degree is unknown. Very little ground-based experimental data is available to provide guidance on forced transition through the use of discrete compression corners, and certainly less flight experience. To be conservative, the decision was made to force transition through the use of a passive (inert) trip array on the first ramp to ensure, at the very least, turbulent flow into the inlet, and also provide some flow spillage relief at the first ramp corner.

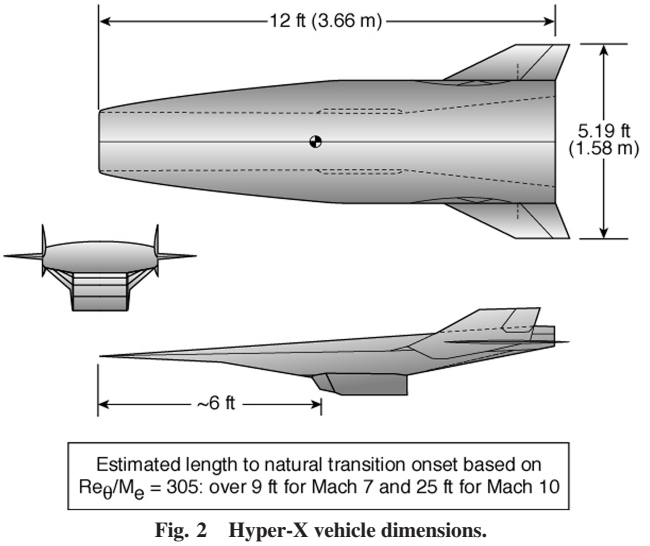

Fig. 2 Hyper-X vehicle dimensions.

B. Hyper-X Trips

The design of the Hyper-X trips was predicated on empirical *rules-of-thumb* that were used to reduce the size of the experimental matrix. First, the general empirical design criteria dictated that the tripping mechanism most effective in forcing hypersonic transition required the formation of streamwise vorticity on a scale within the boundary layer. Thus, the strategy was to create a series of counter-rotating vortex pairs emanating from a spanwise array of trip elements, essentially vortex generators (VG), which were moderately smaller than the predicted boundary-layer height. Initial analysis of the candidate trip configurations determined that, due to their relatively small size, the associated drag penalty to the vehicle would be minimal [9]. The placement of the array, downstream of the vehicle leading edge, was selected to be in the vicinity of a local Mach number at the boundary-layer edge (M_e) of less than four [11]. While M_e rises rapidly near the leading edge, the first forebody ramp provides a wide domain of acceptable edge conditions. For both vehicles, the midpoint on the first ramp was selected as a compromise between locations close to the leading edge where M_e would be low and locations away from the leading edge where the substructure would be thicker and could easily accommodate the trip insert.

A lateral VG array on the first ramp of the Hyper-X lower surface forebody was selected as the approach for tripping the boundary layer for the Mach 7 and 10 flight vehicles. Boundary-layer thickness was selected as the primary dimension with which to size and scale each unit-VG. Based on the ground-based data, a boundary-layer trip height (k) over the boundary-layer thickness (δ) of 0.6 was adequate to bring transition onset onto the first ramp and was used to size the Mach 7 flight vehicle trips, while a $k/\delta = 1.0$ was implemented for the Mach 10 vehicle [7]. This simple approach was deemed

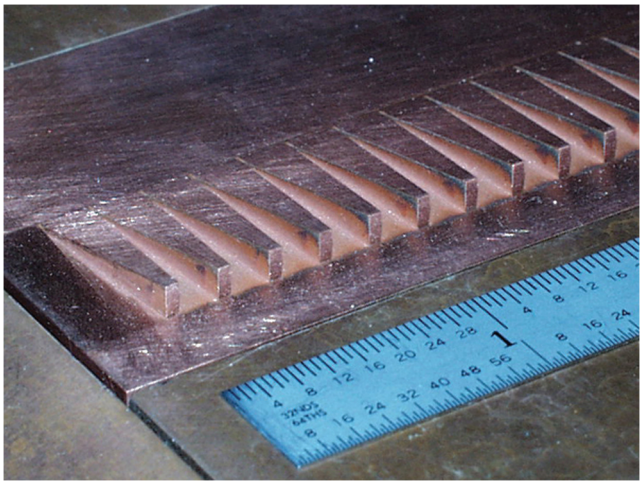

Fig. 3 Close-up photograph of the boundary-layer trips for Mach 7 flight.

acceptable due to the ground-based data being at a similar length Reynolds number as flight.

Specifically, the approach taken to scale the wind-tunnel results to flight was based on k/δ and included an assessment of the forebody boundary-layer thickness for expected variations of the vehicle trajectory, angle of attack α, and wall temperature T_w in flight. Mach 7 flight dispersions at the time of the trip design called for $\alpha = 2\,\text{deg} \pm 1\,\text{deg}$ and wall temperatures between 1000 and 1500°R. A maximum and minimum boundary-layer thickness were computed from these dispersions and determined to be $\delta_{\max} = 0.205$in. and $\delta_{\min} = 0.173$in.. A trip height of $k = 0.125$in. provided an acceptable coverage of 60–70% of the boundary layer. This range was deemed adequate to force transition in a reasonably short distance behind the trip [12], while not excessively enhancing the integrated closed-cowl heat load. Figure 3 provides a close-up photograph of the selected trip design, sized for the Mach 7 vehicle and installed on a full-scale prototype engine test stand (note the flow direction for this photo is roughly upper left to lower right). The successful flights now provide the unique opportunity to verify the trip design and the method by which the trip design was scaled to flight, as well as the natural transition criteria based on the upper surface results. A similar dispersion analysis was used for sizing the final trips for the Mach 10 flight, except as stated before a k/δ of 1 was employed based on the Mach 10 wind-tunnel results. The trip geometry was scaled up from the Mach 7 design to be 0.26-in. high, which allowed for acceptable coverage of 100% of the predicted boundary-layer height when the dispersions were considered.

II. Flight Instrumentation

A. Sensor Locations

Figures 4 and 5 illustrate the Hyper-X research vehicle upper and lower surface showing the location of pressure and temperature instrumentation for both vehicles. Details of the flight instrumentation can be found in [13]. The thermocouples of interest for the present analysis are highlighted in yellow. On the lower surface, only the eight thermocouples along the centerline on the second and third ramps (T201, T003, T204, T207, T005, T208, T006, and T209) were considered, as these gauges were all imbedded thermocouples just slightly below the surface of the Shuttle-like thermal protection system (TPS) tiles. The two thermocouples shown on the lower surface first ramp (T022 and T002) were installed on the tungsten ballast section. These sensors responded differently due to the heat absorption of the thermal mass, thereby requiring a different thermal model to analyze these results. T002 was monitored, however, as an indicator of the local surface temperature along the Tungsten section for the boundary-layer calculations, along with the first two gauges on the second ramp, T201 and T003. Also, the thermocouples shown in Fig. 4 toward the aft part of the forebody (T007–T011) were also

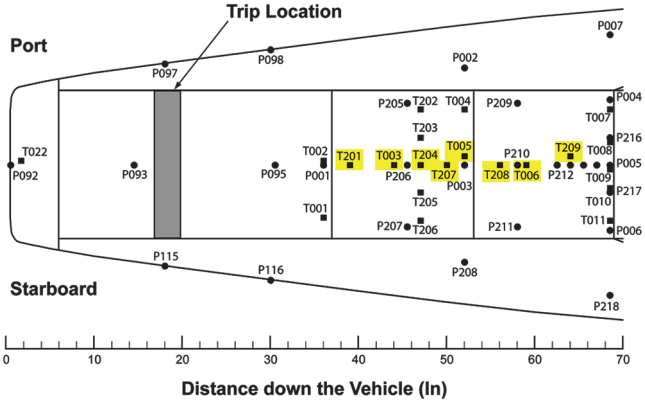

Fig. 4 Lower forebody surface instrumentation layout for both flight vehicles.

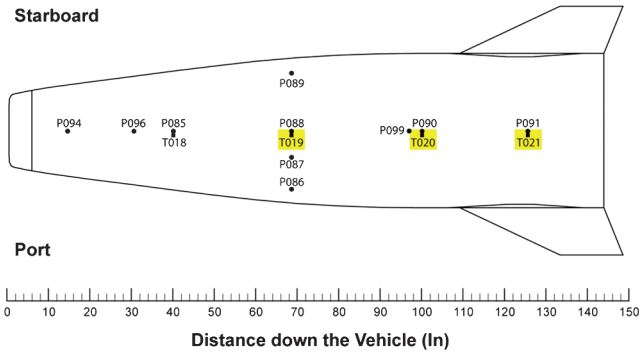

Fig. 5 Upper surface instrumentation layout for both flight vehicles.

installed in a metallic region and for that reason were not analyzed for the present study. On the upper surface (Fig. 5), only the three TPS-installed gauges along the centerline (T019, T020, and T021) were analyzed as T018 was also located on tungsten. This set of 11 similarly installed thermocouples was sufficient to determine the movement of boundary-layer transition for both flights.

B. Thermocouple Installation

The surface temperatures were measured using 0.010-in. diameter type-S thermocouples installed on the alumina enhanced thermal barrier (AETB) tiles. The range and accuracy requirement for these gauges were 490–3100°R and ±3°R, respectively. The AETB tiles, at a nominal density of 12 lb/ft^3, were 6 × 6-in. with the thickness varying between 0.24 and 1.64-in. depending on the tile location on the vehicle. The aerodynamic surface (or outer mold line) of each tile was coated with a diffusion layer made up of toughened unipiece fibrous insulation (TUFI) and AETB, with a penetration depth of 0.1 in. The tiles were bonded to a strain isolation pad (SIP) made of flexible reusable surface insulation material, and in turn bonded to the vehicle structure, using room temperature vulcanizing (RTV)

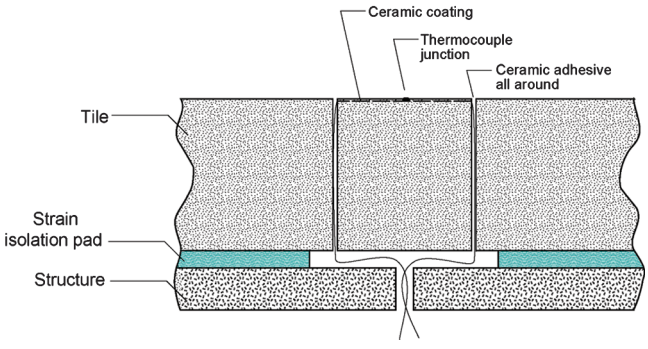

Fig. 6 Typical thermocouple installation in TPS tile (from [13]).

silicone adhesive. Each thermocouple was mounted on the surface of a 0.75-in. diameter AETB ceramic plug, which was installed in the middle of each tile as shown in Fig. 6. The ceramic plugs were coated with a high-emissivity putty material composed of crushed AETB material, borosilicate, an emissivity agent, and tetraorthosilicate. The plugs were mounted flush to the surrounding tile surface. The manufacturer had suggested the nominal thickness of the coating on top of the thermocouple beads to be 0.002-in. Radiographic image analysis of a representative tile equipped with two instrumented plugs, and a more thorough evaluation of thermocouple installation procedures, suggested that the typical thermocouple bead depth was 0.010-in. $\pm$ 0.005. The latter depth was used in the present analysis. The tile surfaces were also equipped with pressure ports for measuring the static surface pressure. The measured static pressures at locations close to thermocouple locations were used in conjunction with thermocouple data to obtain pressure and temperature-dependent thermal properties required for deducing the heating rates from the measured temperatures. Based on these considerations, the time constant for the thermocouples as installed in the tile was estimated to be 0.13 s or better. More detailed information on the tiles and thermocouples can be found in a preliminary report of the Mach 7 flight data [14].

C. Thermal Properties

The thermal properties of SIP, RTV, aluminum and stainless steel were obtained from Williams and Curry [15]. Thermal properties of AETB-12 were obtained from Chiu and Pitts [16][¶]. No thermal or radiant properties were available for the high-emissivity coating applied on top of the AETB ceramic plugs, but the manufacturer had stated that the thermal and radiative response of the coating could be assumed to be similar to the reaction cured borosilicate glass (RCG) coating. RCG thermal and radiative properties [15] for the coating with a thermocouple depth of 0.002-in. had been used in the preliminary report of Mach 7 flight data [14]. Further analysis of the constituents of the coating revealed that using RCG thermal properties is not justified. For the present study, AETB-12 thermal properties and RCG radiative properties were used for the coating, along with a thermocouple depth of 0.010-in. The temperature-dependent RCG emissivity data from Bouslog and Cunnington [17] were used.

III. Postflight Analysis

As mentioned previously, the Hyper-X flight results provide an opportunity to check and refine the engineering tools and methods used to originally design the experiment. The present paper provides just such a review specifically in regards to hypersonic boundary-layer transition. The key steps to the present analysis are: first, conversion of the measured flight temperatures to surface heat transfer rates at each sensor location; second, comparison of the deduced surface heating to all-laminar and all-turbulent heating predictions along the trajectory; third, selection of times of interest corresponding to departure points between the laminar and turbulent trends; and, finally, examination of the calculated boundary-layer properties at these times of interest for comparison to preflight transition criteria and design assumptions.

A. Heat Transfer Analysis

A one-dimensional transient finite volume numerical model was used to analyze heat transfer through the tiles and deduce the surface heating for each thermocouple location. A fully implicit (first-order accurate in time, second-order accurate in space) time marching formulation [18] was used. Previous aeroheating analysis of heating rates from measured surface temperatures on Space Shuttle Orbiter instrumented tiles had ignored the 0.015-in. thick RCG coating in the thermal model and assumed that the measured thermocouple data were at the aerodynamic surface [19]. This assumption had not introduced significant error because of high thermal conductivity of RCG coating. For the present study, the coating was modeled in the thermal analysis. The first node was located on the aerodynamic surface, and the second node at the thermocouple location (0.010-in. below the surface). The measured temperature at node 2 and adiabatic conditions at the backface (structure) were used as the boundary conditions to obtain temperature distributions in the tile from node 3 to the structure at each instant of time. Then, fully implicit finite volume formulation of energy balances, which includes all three (convection, radiative, and conduction) terms, at nodes 2 and 1 were used to calculate the surface temperature and aeroheating rates at each time step, respectively. Additional details on the numerical heat transfer analysis can be found in [14].

1. Data Processing

The measured temperature and pressure data, recorded at 25 Hz, were subjected to two data processing steps before proceeding to the heating analysis: spurious data removal and smoothing. These steps were similar to the data processing used for calculating heating rates on the Space Shuttle Orbiter [19]. Outlying data points that were significantly different than the neighboring data points on either side, were replaced with preceding valid data points. A Hamming window filter [20] using a filter kernel length of 50, or 2 s of data, was used to smooth the recorded temperature and pressure data.

2. Uncertainty Assessment

Because of the limited number of thermocouples available, only 1-D (through the tile thickness) heat transfer was modeled in determining the heating rates. Lateral conduction due to the presence of surface heating gradients and material variations could lead to errors in the calculated heating rates from 1-D analysis [21]. The main sources of uncertainty considered in this study were due to the high-emissivity coating applied on top of the ceramic plugs, specifically the sensor depth and the thermal and radiative properties of the coating. The heating rate RMS uncertainties due to various sources of uncertainty were estimated to be 3.5% due to the $\pm$0.005 uncertainty in thermocouple depth, 15.1% due to use of AETB versus TUFI/AETB diffusion layer thermal properties for the coating, and 5.2% due to the use of temperature-dependent versus constant-temperature RCG emissivity. The overall RMS uncertainty in heating rates due to the combination of the individual sources of uncertainty was estimated to be 16.3%.

B. Engineering Analysis

An engineering code, MINIVER [22], was used to assist in determining boundary-layer transition times during the flight. MINIVER is a versatile engineering code that uses various well-known approximate heating methods, together with simplified flowfields and geometric shapes to model aeroheating environments for aerospace vehicles that operate in the hypersonic flight regime. MINIVER is suitable for research at the conceptual and preliminary design level, and is widely used by NASA, military, academic, and commercial aerospace organizations throughout the U.S. The version of the code used for this study is the in-house NASA Langley Research Center version, which includes numerous operational advantages not available in the official government release, which was last updated in 1991.

Postshock and local flow properties based on normal-shock or sharp-cone/wedge entropy conditions are determined in MINIVER through user selection of the various shock shape and pressure options. The calculations can be based on perfect-gas or equilibrium-air chemistry. Angle-of-attack effects are simulated either through the use of an equivalent tangent-cone or an approximate crossflow option [23]. The flow can be calculated for either two- or three-dimensional surfaces. However, the three-dimensional effects are available only through the use of the Mangler transformation for flat-plate to sharp-cone conditions. Over the last three decades, MINIVER has been used extensively as a preliminary design tool in government and industry and has demonstrated excellent agreement

[¶]Data available from the TPSX Material Properties Database at http://tpsx.arc.nasa.gov [accessed Sept. 2010].

with more detailed solutions for stagnation and windward acreage areas on a wide variety of vehicle configurations, including the Space Shuttle Orbiter, HL-20 [24], X-33 [25] (winged body, lifting body, and vertical lander), X-34 [26], X-37 [27], X-43 and NASP. The principal advantage of this engineering code over some of the more detailed methods is the speed with which the analyses can be performed for each flow condition along a trajectory. Its strength lies in its ability to quickly provide the transient aeroheating environments required for TPS analysis and sizing.

In this investigation MINIVER was used to develop an estimate of the laminar and turbulent heating levels for a given body point along the best-estimated trajectory (BET) for each flight. Vehicle locations, on both the upper and lower surfaces, were modeled using Eckert flat-plate heating methods [28], Blasius skin friction (laminar) and Schultz–Grunow (turbulent) skin friction methods, and assuming wedge flow conditions at the equivalent angle of attack for each thermocouple location (eight lower surface and three upper surface). A radiation equilibrium temperature based on temperature-dependent emissivity data [17] was used as the wall temperature boundary condition. In addition to the fully laminar calculations, transition onset conditions were considered at the nose (0 in.), an approximate trip location (17 in.), and at the start of 2nd ramp (37.3 in.). A limited time-step sensitivity study was performed to ensure that transient heating events were captured with minimal overshoot, which resulted in a time-step interval selection of 0.25 s that roughly corresponds to the frequency response of the thermocouples. For the sake of discussion within this paper, the MINIVER laminar and turbulent heating predictions are only intended to provide guidance for determining the local boundary-layer state by comparison against the reduced heating determined from the measured temperatures. No implication as to the accuracy of the predicted heating levels from MINIVER are intended, as the absolute values are provided only for reference by which the trajectory points are identified that correspond to times of transition between the laminar and turbulent limits.

C. Computational Analysis and Assumptions

The boundary-layer code of Anderson and Lewis [29], which was originally used in the design of the boundary-layer trips for flight [12], was also used for the present analysis. The code was run with a simplified geometry (two-dimensional flat plates with sharp leading edge) and an input Mach number, freestream pressure, freestream temperature, and wall temperature. All computations were based on a fully laminar boundary layer. The Anderson code uses a definition of 99.5% of freestream velocity to establish the boundary-layer thickness. As a check, computations were run with the same inputs as the original design effort and the results were identical. The geometry used in this study was the vehicle centerline for the top and bottom surfaces of the X-43A configuration with the cowl closed. The bottom surface was only run to 37-in. because that was sufficient to capture the boundary-layer trips and the region downstream where tripping would occur. The boundary-layer trip leading edge was at an axial location of 18.5-in. (see Fig. 4). The top surface was run all the way to the vehicle base. All coordinate systems are based on [30].

As noted earlier, a goal of the present analysis is to verify the methods used during design and as such the same tools and assumptions were employed here as was done during the design of the flight trips. For the earlier effort, a simplifying assumption of modeling the leading edge as sharp was employed and then accounted for by comparison of the calculated boundary-layer thickness from the boundary-layer code to separate results obtained via viscous computational fluid dynamics (CFD) solutions in which the leading edge bluntness was modeled (see [12]). For consistency, the same approach was employed here. Bittner [31] provides for the Mach 7 case the details of the comparison between the three-dimensional Navier–Stokes (GASP) results and the present two-dimensional, sharp boundary-layer code results, and only a summary discussion is included here. The comparison of the momentum thickness Reynolds number divided by the edge Mach number between the two computations showed nearly identical results over the first 30 in. of the vehicle, followed by slow departure of results with distance perhaps due to three-dimensional effects. On the other hand, the difference in boundary-layer thickness was more significant, with as much as a 35% disagreement at the trip station. The present difference, a 0.050-in. underprediction by the boundary-layer code, was nearly identical to the noted bluntness increment used previously during the design analysis. The conditions associated with the design analysis were different than the present comparison, and thus in both cases the difference between the CFD and boundary-layer solutions are interpreted to be a direct result of bluntness. For the Mach 10 case, a separate two-dimensional GASP analysis was recently completed for both sharp and blunt leading edges at two representative wall temperatures. Based on the results of this analysis, a bluntness increment of 0.12-in. was determined to account for the Mach 10 sharp-to-blunt differences. Although one could call into question such an *engineering style* approach for accounting for nose bluntness, the pertinent question for the subsequent analysis is how well did this approach work in designing the flight hardware.

On the upper surface, the local temperatures at each gauge were known based on the measured data. However, due to the limited spatial resolution of the temperature variation across the surface, the boundary-layer analysis was conducted with a constant wall temperature. Also, the lower surface did not have a sensor in the vicinity of the trips on the first ramp, which was on the tungsten section. For these reasons, wall temperature effects were assessed in the present analysis by computing results at a constant wall temperature of 800°R for comparison at a consistent wall temperature, as well as for any noted range in measured surface temperatures. Note that for the lower surface, T002 was selected as the representative wall temperature near the trips. The computed variation based on the wall temperature range will be noted where appropriate either by discussion or with an uncertainty number in the figures.

IV. Mach 7 Flight Results

A. Temperature Measurements

Figure 7 provides the lower and upper surface temperature measurements for the centerline thermocouples listed sequentially by position down the body (lower first, then upper) during the first 500 s of the Mach 7 flight trajectory. Times are based on the release of the Hyper-X Launch Vehicle (Research Vehicle plus Pegasus booster) from the B-52. Separation from the booster occurred at approximately 92 s after drop, while cowl open and engine ignition was at roughly 96 s. On the lower surface (open symbols), the measured temperatures all show roughly the same trends, all within a couple of hundred degrees of each other. The peak temperature measured on the lower surface was 2200°R for T208, which is near the beginning of the third ramp. With the exception of the slight temperature deviation, for gauges T201 and T003 at around 80 s (noted as a *Temperature Drop?* in Fig. 7), the trends are identical and might suggest the lower surface stayed turbulent during the entire

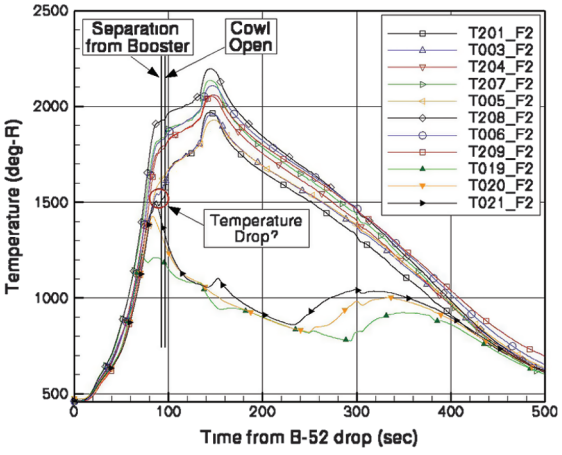

Fig. 7 Surface temperature measurements for Mach 7 Hyper-X flight.

trajectory. On the other hand, the upper surface (filled symbols) shows a distinct and systematic departure from the rising lower surface temperatures. The temperatures on the upper surface stabilize at a level dramatically lower than that observed on the lower surface before systematically increasing at around 250 s into the trajectory. This may be an indication that the upper surface was fully laminar during the powered scramjet portion of the trajectory.

B. Flight Heating Results

The results of the heating analysis for the Mach 7 flight, based on the assumptions and properties listed previously, are shown in Fig. 8 for both the lower and upper surfaces. Also plotted on this figure are proposed trajectory points identified for the subsequent boundary-layer analysis, which were originally identified as part of a preliminary analysis detailed in [14]. As mentioned previously with the temperature plots, the lower surface heating trends were all similar, with the exception of T201 and T003, which for a brief period of time between 78 and 95 s diverge noticeably from the others. These two times are identified in Fig. 8 as trajectory points 2 and 4 (TP2 and TP4). Also shown is TP5, an unclassified representative of the nominal test point (similar angle of attack and flow conditions but before the cowl opened). On the upper surface there is a systematic and precipitous drop in heating starting at 70 s (TP1) for thermocouple T019, and then at 83 s (TP3) for T021. The point at which the heating begins to drop is interpreted as the end of fully turbulent conditions at that sensor, which will be substantiated further in a following section. Conversely, later there is a systematic rise in heating, first starting with T021 at 232 s (TP7), then T020 at 268 s (TP8), and finally T019 at 293 s (TP9), which is interpreted as the forward movement of transition onset. There is one other brief rise in the heating levels for T021 at 141 s that also may be a transition event (TP6). Based on the present in-depth heating analysis, the deduced temperature at the surface had a peak value of 85.7°R higher than the measured flight thermocouple data plotted in Fig. 7 with a corresponding RMS deviation for the entire trajectory and all 11 thermocouples of 20.9°R. Note that the selection of times for each trajectory point was somewhat subjective, thus a time sensitivity study was conducted and these results will be discussed in a subsequent section.

C. Heating Level Assessment

As an initial guide for determining the state of the boundary layer during the Mach 7 flight, the reduced heating rates from the measured temperature response for each thermocouple were compared against the corresponding MINIVER predictions as a function of time from the B-52 drop. Two representative comparisons are provided in Figs. 9 and 10, for the upper and lower surfaces, respectively. For the upper surface, the heating results for T021 initially appear to be closer to the MINIVER calculated turbulent heating profile (for an assumed all-turbulent case with transition at the nose), and then drops down to the all-laminar calculated profile. The departure point is shown in Fig. 9 to be 83 s, which corresponds to the end of fully turbulent conditions at the aft end of the upper surface, and the time at which the heating level appears all-laminar is 112 s. The departure from the laminar predicted profile is also shown to be 232 s, with fully turbulent conditions at 338 s. For the lower surface, Fig. 10, the reduced heating profile appears to be closer to the predicted turbulent

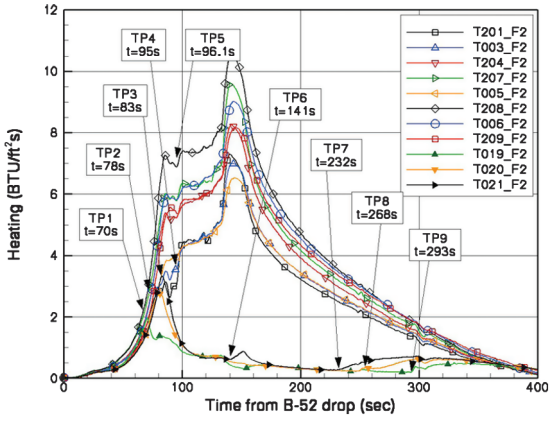

Fig. 8 Reduced surface heating for Mach 7 Hyper-X flight.

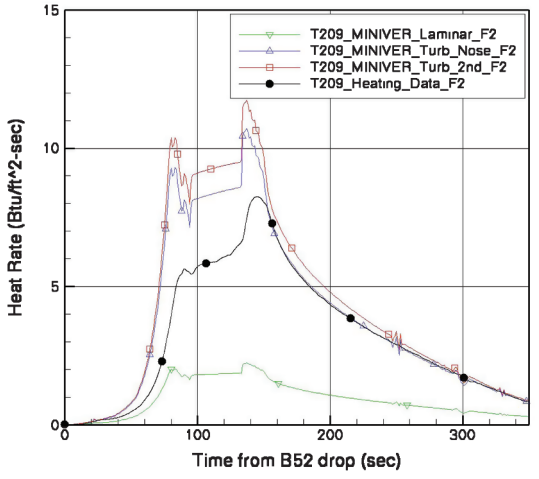

Fig. 10 Comparison of reduced T209 lower surface heating to MINIVER predictions for Mach 7 flight.

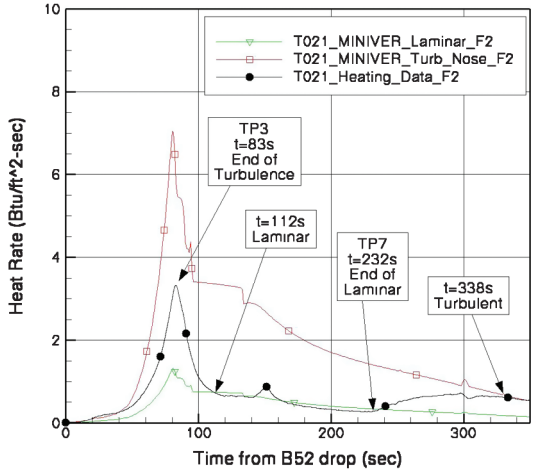

Fig. 9 Comparison of reduced T021 upper surface heating to MINIVER predictions for Mach 7 flight.

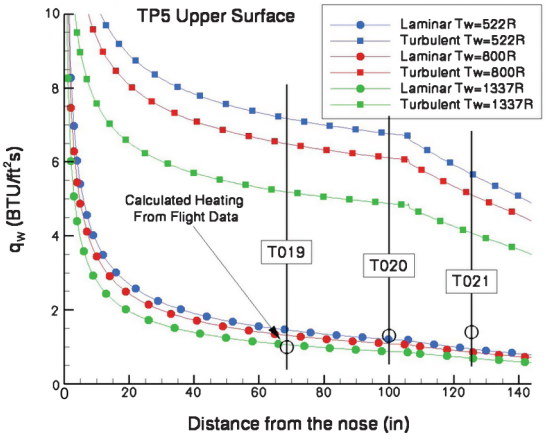

Fig. 11 Comparison of Mach 7 flight upper surface heating to BL code predictions at 96 s.

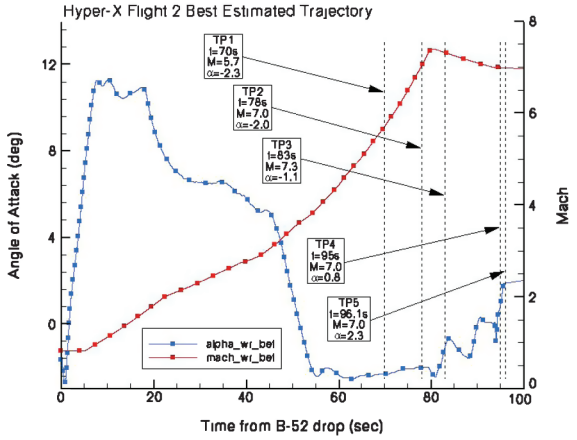

Fig. 12 Mach 7 trajectory points for boundary-layer analysis on ascent.

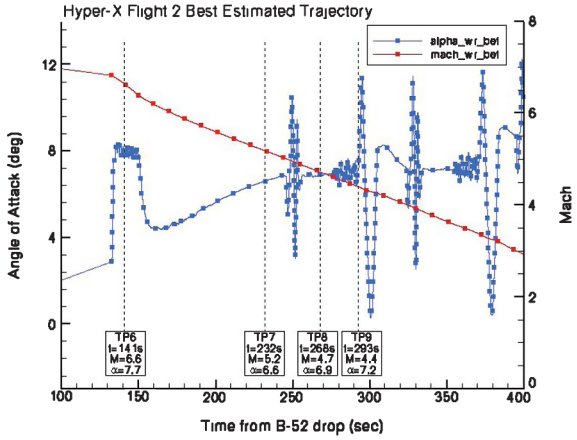

Fig. 13 Mach 7 trajectory points for boundary-layer analysis on descent.

heating results from MINIVER for most of the trajectory. Note that for the lower surface, turbulent predictions were completed for both fully turbulent from the nose and transition starting at the start of the second ramp to see if transition onset location could explain some of the differences between measured and predicted.

A further comparison of the reduced heating rates from the flight data to the predicted laminar and turbulent heating (now based on the results from the Anderson boundary-layer code) for TP5, for the range of measured temperatures on the upper surface, are shown in Fig. 11. As can be seen with this comparison, the heating rates for the upper surface at $t = 96$ s are in much closer agreement to the laminar predictions from the boundary-layer code. Note that the rising trend in flight heating rates are due to the aft gauges still being in a transitional state, not yet recovered from turbulent conditions, which for T021 occurs at 112 s (see Fig. 9). Knowing that the upper surface is mostly laminar at the nominal test point anchors the rest of the trajectory points, as TP1 and TP3 would similarly have to correspond to the end of turbulence for the upper surface, while TP7 through TP9 would represent transition onset during descent. At the same time the lower surface heating rates (Fig. 8) are on the order 5–6 times higher than the laminar values on the upper surface and are shown to be similar to the predicted turbulent levels from MINIVER (Fig. 10). Thus, the evidence tends to support that the lower surface (with the possible exception of T201 and T003 for the brief period between TP2 and TP4) remained turbulent during the entire trajectory, while the upper surface was laminar for over 120 s (including the powered scramjet portion) of the trajectory. Note that this determination of the boundary-layer state is based on the comparisons to the laminar and turbulent *trends* from MINIVER and not the absolute values.

D. Trajectory Information

The trajectory points of interest (for the subsequent calculation of boundary-layer properties), with the times previously identified from the heating plots, are now established in Figs. 12 and 13 during ascent and descent, respectively. The figures do not include any *real* trajectory information during the open cowl (classified) portion of the trajectory, but instead shows a straight line connecting the two unclassified sections. Descriptions of the underlying basis for each of the nine trajectory points are described in Table 1, along with key flow conditions required for the subsequent boundary-layer analysis as determined from the BET v2.3 [32]. Note that the version number denotes that this trajectory is the third (and most recent) release of the BET for the second flight. There are four ascent points (two each based on the upper and lower surface), one point just before the cowl opens (representing the unclassified test point), and four descent points (all based on the upper surface). Times are listed referenced to the sensed drop of the Hyper-X Launch Vehicle.

V. Mach 10 Flight Results

A. Temperature Measurements

Figure 14 provides the lower and upper temperature measurements for the centerline thermocouples listed sequentially by position down the body (lower first, then upper) during the first 800 s of the Mach 10 flight trajectory. Times again are based on the release of the Hyper-X Launch Vehicle from the B-52. Separation from the booster occurred at approximately 88 s after drop, while cowl open and engine ignition was at roughly 92 s. On the lower surface, most of the measured temperatures all show roughly the same trends, all within a couple hundred degrees of each other, except for T201 (the furthest forward sensor), which seems to behave differently from the others. The peak temperature measured on the lower surface was 2880°R for T006, which is near the beginning of the third ramp. All of the sensors, both upper and lower, appear to suggest significant temperature fluctuations that begin at around 80 s, after which most of the lower surface temperatures appear to rise sharply while the upper surface temperatures decrease slightly. As mentioned earlier, T201 is an outlier that takes a while (until about 276 s) to reach the same trends as the other lower surface sensors. Similar to the Mach 7 flight, the upper surface for the Mach 10 flight shows a distinct and systematic departure from the quickly rising temperatures (initially of the same magnitude as the lower surface) that stabilizes roughly around 1000°R before systematically increasing at around 400 s into the trajectory. This suggests that the upper surface was fully laminar

Table 1 Mach 7 trajectory points for boundary-layer analysis

Trajectory point	Time, s	α, deg	Mach	P_∞, psf	T_∞, R	Surface: event description
1	70	−2.317	5.719	62.46	389.2	Upper: T019 indicates laminar onset?
2	78	−2.038	7.040	45.00	396.9	Lower: T201 & T003 appear nonturbulent?
3	83	−1.077	7.318	37.77	399.7	Upper: T021 indicates laminar onset?
4	95	0.844	6.989	29.88	402.1	Lower: T201 & T003 return to turbulent?
5	96.1	2.329	6.975	29.52	402.2	Lower: Approximate nominal angle of attack
6	141	7.684	6.639	42.45	397.3	Upper: T021 shows heating rise?
7	232	6.593	5.185	41.02	397.9	Upper: T021 indicates transition onset?
8	268	6.881	4.720	48.51	396.3	Upper: T020 indicates transition onset?
9	293	7.199	4.397	55.46	394.4	Upper: T019 indicates transition onset?

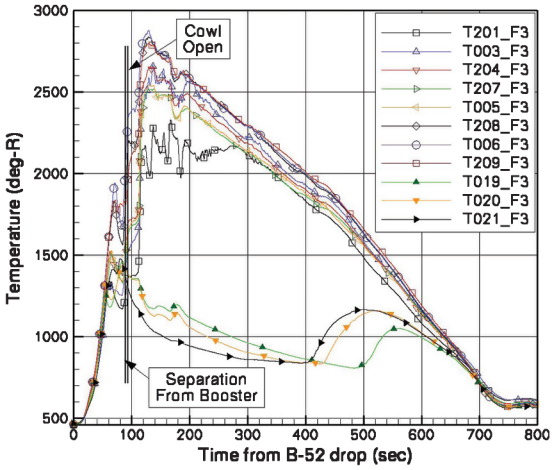

Fig. 14 Surface temperature measurements for Mach 10 Hyper-X flight.

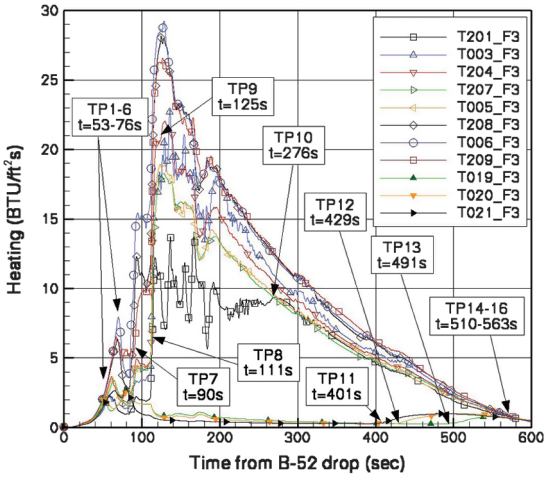

Fig. 15 Reduced surface heating for Mach 10 Hyper-X flight.

during the powered scramjet portion of the trajectory. The lower surface, however, is a little harder to interpret based on the measured temperatures.

B. Flight Heating Results

The results of the heating analysis for the Mach 10 flight, consistent with the assumptions and properties of the Mach 7 case, are shown in Fig. 15 for both the lower (open symbols) and upper (closed symbols) surfaces. Also plotted on this figure are proposed trajectory points identified for the subsequent boundary-layer analysis. As mentioned previously with the temperature plots, the lower surface heating trends were all similar, with the exception of T201, which for a period of time between 55 and 276 s diverge noticeably from the others. These 2 times were designated as trajectory points 2 and 10, as listed in Table 2. Also shown in Fig. 15 is trajectory point 7, an unclassified representative of the nominal test point (similar angle of attack and flow conditions but before the cowl opened). On the upper surface there is a systematic and precipitous drop in heating starting at 53 s (TP1) for thermocouple T019, and then at 66 s (TP4) for T021. The heating drop is interpreted as the end of turbulence for each location, and will be substantiated further in a following section. Conversely, later there is a systematic rise in heating, first starting with T021 at 401 s (TP11), then T020 at 429 s (TP12), and finally T019 at 491 s (TP13), which is interpreted as the forward movement of transition on set. All of the sensors show a significant drop in the heating levels between 55 and 90 s (TP2–TP7), which could indicate that the lower surface was briefly laminar. Based on the present in-depth heating analysis, the deduced temperatures at the surface was at most 165.8°R higher than the measured flight thermocouple data plotted in Fig. 14 with a corresponding RMS deviation for the entire trajectory and all 11 thermocouples of 24.2°R.

C. Heating Level Assessment

Again, the reduced heating rates from the measured temperature response for each thermocouple were compared against the corresponding MINIVER prediction as a function of time from the B-52 drop to determining the state of the boundary layer during the Mach 10 flight. Three representative comparisons for the upper and lower surfaces are provided in Figs. 16–18. In this case 2 lower surface comparisons are provided to help classify the boundary-layer status close to the trip station (T201) and close to the engine inlet (T209). For the upper surface, the heating results for T021 initially are closer to the MINIVER calculated turbulent heating profile (for an assumed all-turbulent case with transition at the nose), and then drops down to the all-laminar calculated profile. The departure point is shown in Fig. 16 to be 66 s (TP4), which was previously identified as the end of turbulence (or onset of laminar) point and the time at which the heating level appears all laminar is 76 s (TP6). The departure from the laminar predicted profile is also shown to be 401 s (TP11), with fully turbulent conditions at 510 s (TP14). For T209 on the lower surface, Fig. 17, the reduced heating is also initially close to the predicted turbulent heating results from MINIVER, with an abrupt departure at 69 s that plateaus at a laminar-like level at 75 s. The surface heating then increases, starting at 90 s, to the same level of the turbulent MINIVER predictions at 125 s. For T201 on the lower surface, Fig. 18, the departure from the turbulent levels occurs at 55 s, reaches laminar levels at 82 s, and then a sharp rise toward the turbulent predictions starts at 110 s, but does not reach the turbulent profile until 276 s. The times identified in Figs. 17 and 18 should provide the

Table 2 Mach 10 trajectory points for boundary-layer analysis

Trajectory point	Time, s	α, deg	Mach	P_∞, psf	T_∞, R	Surface: event description
1	53	−3.38	5.57	61.57	386.6	Upper: T019 turbulent to laminar
2	55	−3.21	5.86	54.34	392.2	Both: T020 and T201 turbulent to laminar
3	62	−2.85	7.03	36.10	392.7	Upper: T019 laminar
4	66	−2.83	7.75	29.45	397.5	Upper: T020 laminar and T021 turbulent to laminar
5	72	−2.83	8.98	22.35	400.1	Lower: T209 turbulent to laminar
6	76	−2.86	9.90	19.08	404.8	Both: T021, T201, T209 laminar
7	90	1.40	9.69	14.18	411.1	Lower: T209 laminar to turbulent
8	111	1.01	9.62	14.17	411.1	Lower: T201 laminar to turbulent
9	125	5.79	9.44	16.49	405.9	Lower: T209 turbulent
10	276	6.19	7.27	23.58	399.9	Lower: T201 turbulent
11	401	6.79	5.87	35.27	393.3	Upper: T021 laminar to turbulent
12	429	6.10	5.54	40.09	394.6	Upper: T020 laminar to turbulent
13	491	6.32	4.82	54.49	391.9	Upper: T019 laminar to turbulent
14	510	6.29	4.61	60.19	387.4	Upper: T021 turbulent
15	525	6.81	4.43	65.16	385.7	Upper: T020 turbulent
16	563	6.48	3.91	79.66	385.7	Upper: T019 turbulent

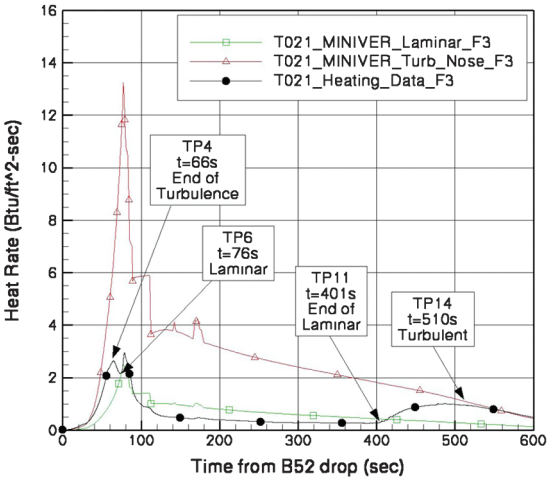

Fig. 16 Comparison of reduced T021 heating to MINIVER predictions for Mach 10 flight.

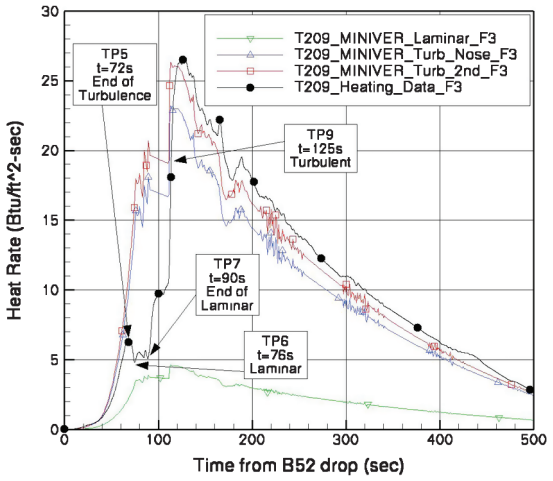

Fig. 17 Comparison of reduced T209 heating to MINIVER predictions for Mach 10 flight.

information needed to identify the boundary-layer conditions associated with the trips being fully effective and incipient.

Figure 19 provides a comparison of the reduced heating rates from the flight data to the laminar and turbulent heating predicted from the boundary-layer code for TP7 for the range of measured temperatures

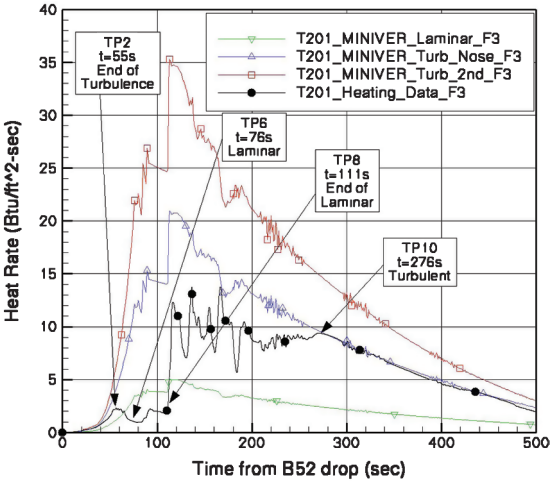

Fig. 18 Comparison of reduced T201 heating to MINIVER predictions for Mach 10 flight.

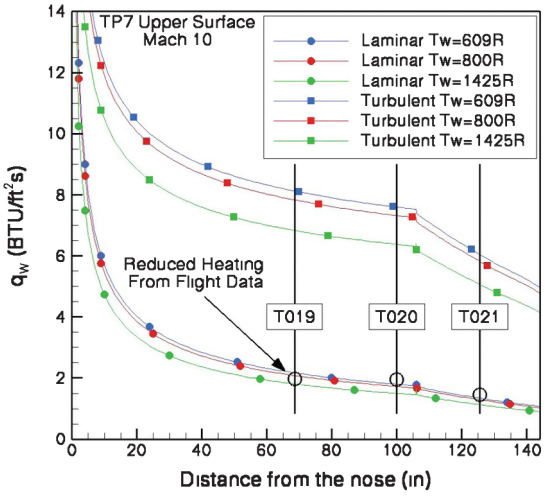

Fig. 19 Comparison of Mach 10 flight heating rates to BL code predictions.

on the upper surface. As can be seen with this comparison, the heating rates for the upper surface at 90 s are in close agreement with laminar predictions from the boundary-layer code. Again, with the knowledge that the upper surface is laminar at the nominal test point anchors the rest of the trajectory points, as TP1 and TP2 would have to correspond to the end of turbulence for the upper surface on ascent, while TP11 through TP13 would represent transition onset during descent. For the lower surface, the heating rates (Fig. 15) at 90 s are only on the order 2 times higher than the laminar values on the upper surface and are shown to also be laminar levels (or nearly so) from MINIVER (Fig. 17). Thus, the evidence suggests that the lower surface was briefly laminar, or at least not turbulent, just in front of the inlet between 69 and 90 s (which is just before the engine cowl opening), and transitional during the engine test. The upper surface was laminar for over 325 s (including the powered scramjet portion) of the trajectory.

D. Trajectory Information

The trajectory points of interest, with the times previously identified from the heating plots, are now established in Figs. 20 and 21 during ascent and descent, respectively. The figures do not include any *real* trajectory information during the open cowl (classified) portion of the trajectory, but instead shows a straight line connecting the two unclassified sections. Descriptions of the underlying basis for each of the 16 trajectory points are described in Table 2, along with key flow conditions required for the subsequent boundary-layer analysis as determined from the BET v3.1 [33]. Note that the version number denotes that this trajectory is the first release of the BET for

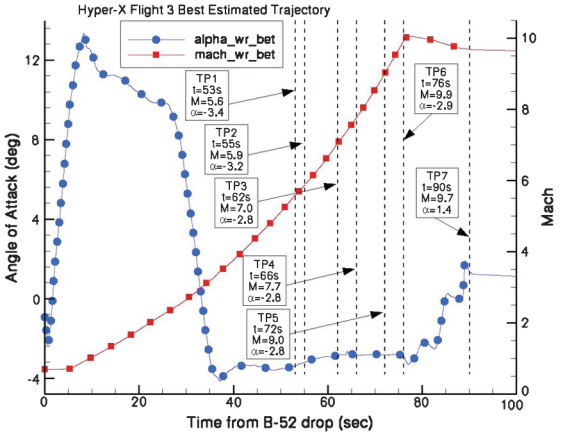

Fig. 20 Mach 10 trajectory points for boundary-layer analysis on ascent.

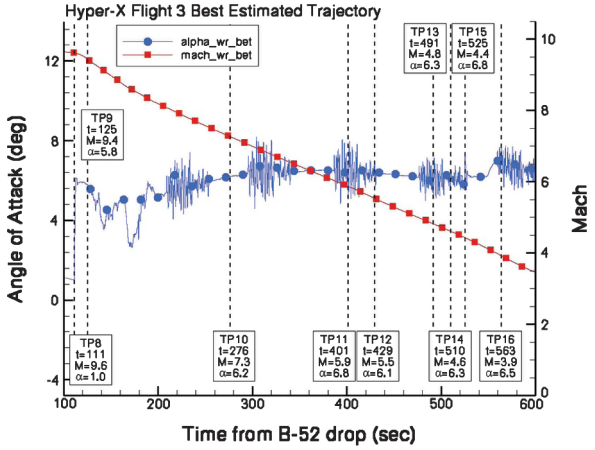

Fig. 21 Mach 10 trajectory points for boundary-layer analysis on descent.

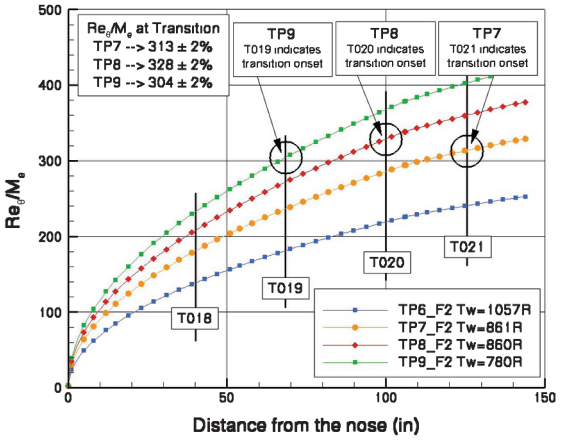

Fig. 23 Upper surface Re_θ/M_e for Mach 7 Trajectory Points 6–9.

the third flight. There are six ascent points, one point just before the cowl opens (representing the unclassified test point), and nine descent points.

VI. Boundary-Layer Analysis

A. Natural Transition (Upper Surface) Results

Figure 22 shows a plot of Re_θ/M_e as a function of axial distance for the three trajectory points that relate to the top surface during the Mach 7 ascent. The plot indicates the gauge locations via vertical bars with gauge numbers listed. The wall temperatures used were based on the range of measured values on the upper surface at that point on the trajectory. These trajectory points were identified based on the data suggesting the boundary layer was beginning to transition from turbulent to laminar, which provided Re_θ/M_e of 453 for TP1, 420 for TP2, and 393 for TP3. The measured variation in upper surface wall temperatures provides less than a 4% change in the calculated values of Re_θ/M_e. Because during these particular trajectory points the vehicle is experiencing some rapid changes in angle-of-attack and flow conditions, a sensitivity study to small increments in time around TP1 and TP3 was performed. Bittner [31] provides the details of that analysis, where a one or 2 s shift in time for each trajectory point was enough to adjust the results such that these cases overlapped at a value of Re_θ/M_e of 400. Typically a value of 300 is expected for boundary-layer transition onset from laminar to turbulent. Note that TP2 also corresponds to when T019 indicated the start of laminar flow, which provided a lower value of Re_θ/M_e (~350).

Figure 23 shows a similar plot of Re_θ/M_e as a function of axial distance for the trajectory points that relate to the top surface but now during Mach 7 descent. The wall temperature shown was based on the measured value at that location at that point in the trajectory, while the uncertainty variance listed in the figure is based on the range of temperatures on the upper surface. In this case an approximate value of 300 seems appropriate for transition onset from laminar to turbulence, roughly validating the preflight transition criteria for transition onset. The actual values predicted were 313 for trajectory point 7, 328 for trajectory point 8, and 304 for trajectory point 9, with roughly a 2% uncertainty spread based on wall temperature. These results indicate that the NASP transition criterion was sufficient to indicate transition from laminar to turbulent flow. Trajectory point 6, which indicated a brief increase in the heating rate, only had a Reynolds number ratio of 240 and probably was not a transition event, but instead related to the high angle-of-attack maneuver shown in Fig. 13.

Figure 24 shows a similar plot of Re_θ/M_e as a function of axial distance for the three trajectory points that relate to the top surface sensor locations first indicating laminar conditions during the Mach 10 ascent. The wall temperatures shown are based on the nominal value for each trajectory point. These trajectory points were identified based on the data suggesting when the boundary layer was first laminar, which provided Re_θ/M_e of 329 for TP3, 345 for TP4, and 290 for TP6. The measured variation in upper surface wall temperatures provides at most a 4% change in the calculated values of Re_θ/M_e. For the trajectory points for which these sensors first showed the departure from turbulent heating rates (TP1, TP2, and TP4), a higher value of Re_θ/M_e, roughly 400, was identified (not shown).

Figure 25 shows a similar plot of Re_θ/M_e as a function of axial distance for the trajectory points that relate to the top surface but now during Mach 10 descent. The calculations shown are based on the nominal wall temperature for each trajectory point. In this case an average value of 280 seems appropriate for the onset of transition

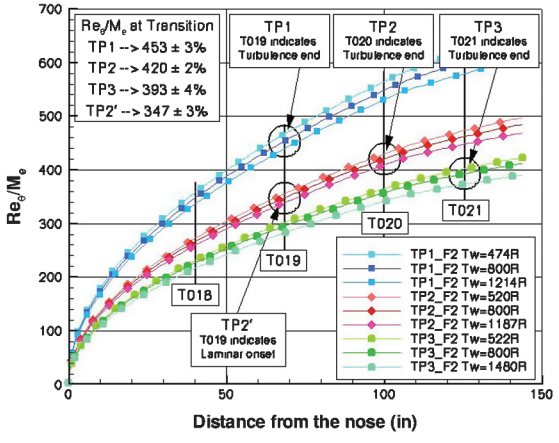

Fig. 22 Upper surface Re_θ/M_e for Mach 7 Trajectory Points 1–3.

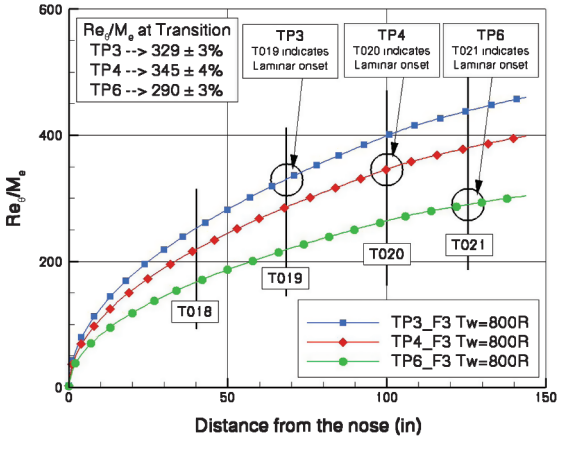

Fig. 24 Upper surface Re_θ/M_e for Mach 10 ascent trajectory points.

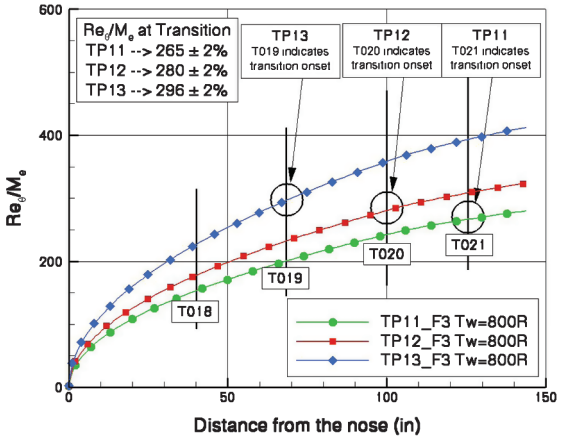

Fig. 25 Upper surface Re_θ/M_e for Mach 10 descent trajectory points.

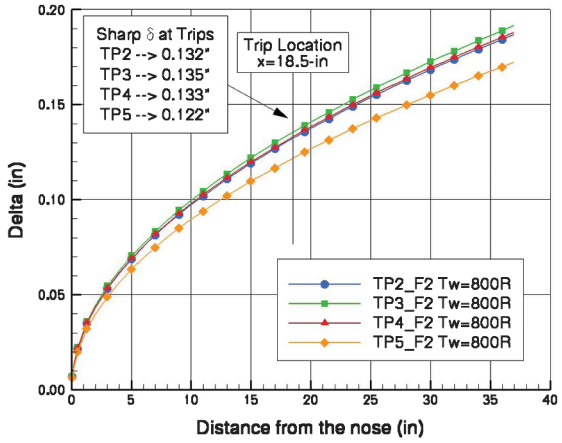

Fig. 27 Boundary-layer thickness calculations for the Mach 7 lower surface.

from laminar to turbulence, which again is slightly lower than the corresponding result during ascent. These Mach 10 descent results are similar to the results identified with the Mach 7 flight data. The actual values predicted were 265 for TP11, 280 for TP12, and 296 for TP13, with roughly a 2% uncertainty spread based on wall temperature. Also, a time sensitivity check was conducted for these Mach 10 descent cases whereby the boundary-layer properties were examined for ±2 seconds around TP11, TP12, and TP13 with only a 4% variance in Re_θ/M_e noted over the 4-second interval. Thus. the Mach 10 results also support the conclusion that the NASP transition criterion is a reasonable approach for estimating the onset of natural transition from laminar to turbulent flow at hypersonic flight conditions.

B. Forced Transition (Lower Surface) Results

Figure 26 shows a plot of the momentum thickness Reynolds number over edge Mach number ratio as a function of axial distance for the Mach 7 trajectory points that relate to the bottom surface (also including TP3). For this comparison, a consistent wall temperature of 800°R was used for each trajectory point. Although not included on the plot, when the range of measured surface temperatures were investigated, only a 3% difference in Re_θ/M_e was noted. Of the trajectory points selected, TP2 and TP4 correspond to when gauges T201 and T003 indicate the beginning and end to brief reduction in heating (interpreted as a reduction in tripping effectiveness), while TP3 represented a trajectory point in between where the effectiveness was the least. TP5 was selected as the unclassified representative of the nominal design point for comparison to the preflight predictions. The actual values predicted at the trip location were 127, 121, 125, and 136 for trajectory points 2, 3, 4, and 5, respectively. The lowest computed value of Re_θ/M_e was for TP3, which qualitatively agrees with the reduced tripping effectiveness trends, while the end points TP2 and TP4 have roughly the same value. Compared with the preflight natural transition criterion ($Re_\theta/M_e = 305$ from NASP), the local values for all four trajectory points were roughly a factor of 3 less than that required for natural transition and thus the first ramp (at the very least) would have likely been laminar, with the resulting laminar separation at the ramp corner, during much of the high Mach number portion of the Mach 7 flight.

The boundary-layer thickness is plotted in Fig. 27 for the same four Mach 7 lower-surface trajectory-points of interest. Once again the values at trajectory points 2 and 4 are about the same at the trip location. For the nominal test point (TP5), the boundary-layer thickness was calculated to be 0.122-in for a wall temperature of 800°R. As stated earlier, the flight trips were sized to have a minimum height of 60% of the boundary-layer thickness [34] considering a 2-deg span of angle-of-attack and additional increments for wall temperature effects and bluntness. The original analysis resulted in a thickness of 0.182-in. for the then-nominal angle of attack of 2-deg with bluntness at a wall temperature of 1000°R and the resultant trip height was 68% of the boundary-layer thickness. Using the bluntness increment (mentioned previously) of 0.050-in. with the calculated boundary-layer thickness for TP5 results in an estimated thickness of 0.172-in., or k/δ of 0.73. The actual test point angle of attack increased from 2.0 to 2.3-deg (the closest angle-of-attack case with the cowl closed), however, the resulting boundary-layer thickness was offset by the measured wall temperature being lower than predicted. Figure 28 shows the sensitivity of boundary-layer thickness to wall temperature. Using the measured temperature at gauge T201 to represent the first ramp, which is not realistic but gives an upward bound, results in a sharp-value boundary-layer thickness of 0.146-in., and with the bluntness increment, 0.192-in. The tungsten section temperature measurement from gauge T002, which

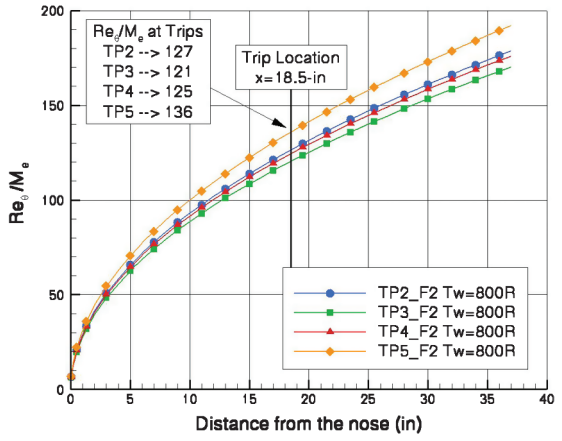

Fig. 26 Lower surface Re_θ/M_e at trips for the Mach 7 trajectory points.

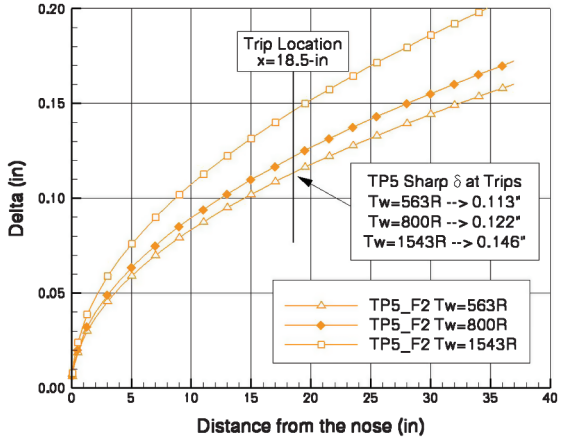

Fig. 28 Boundary-layer thickness sensitivity to temperature variations for Mach 7 lower surface.

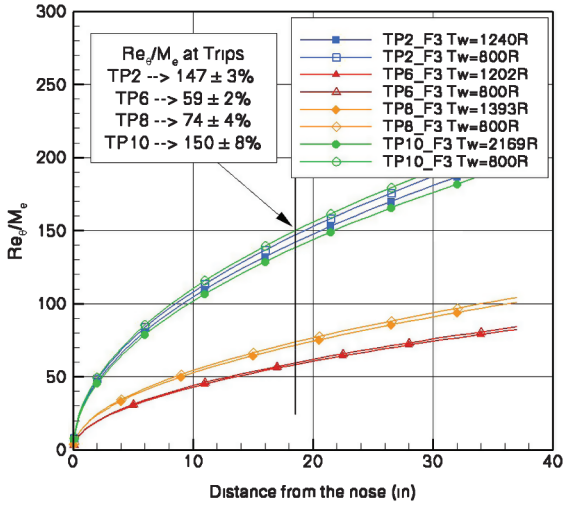

Fig. 29 Mach 10 Reynolds number ratio calculations at the trip station.

is a little low when compared with the preflight predictions (perhaps due to its proximity to the ramp corner), results in the lower bound thickness of 0.113-in., or 0.159-in. with bluntness. Thus, the range of boundary-layer thicknesses (including bluntness) corresponding to the range of potential surface temperatures at the trip station is 0.159–0.192-in., which corresponds to a k/δ range of 65–79%. Based on the present analysis (which purposefully mimicked the design approach) the boundary-layer trip height to boundary-layer ratio was within the target range and the trips performed as designed for the Mach 7 flight.

Figure 29 provides the calculated Re_θ/M_e as a function of the lower surface axial distance for the Mach 10 trajectory points associated with T201. As revealed in Fig. 18, TP2 and TP10 correspond to when the trips were shown to be fully effective (turbulent at the furthest forward measurement location, T201), while TP6 and TP8 correspond to when the trip were shown not to be fully effective (not turbulent at T201). The calculations reveal a distinct shift in Re_θ/M_e between those two groupings. The calculated values for the trip location, based on a consistent wall temperature value of 800°R, were 147, 59, 74, and 150 for trajectory points 2, 6, 8, and 10, respectively. At worst an 8% difference was observed when considering the sensitivity of each of these values to the measured range of wall temperatures.

The corresponding boundary-layer thickness calculations for these T201 Mach 10 trajectory points are shown in Fig. 30. While the groupings in this case are not as distinct, nevertheless the trends suggest a δ threshold, above which the trips are no longer fully effective. As noted previously, these calculations are for a sharp

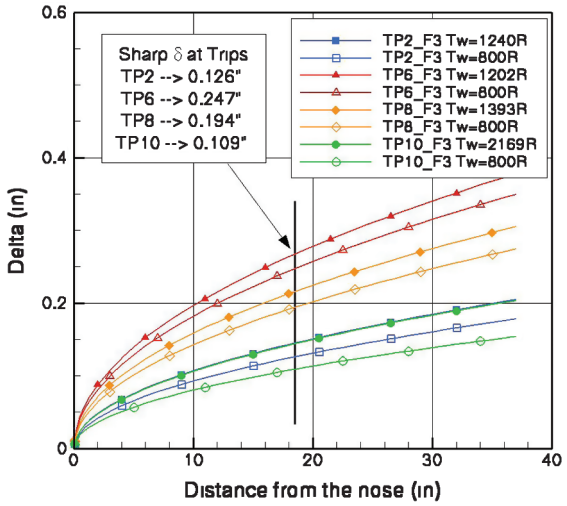

Fig. 30 Mach 10 boundary-layer thickness calculations at the trip station.

leading edge and the bluntness increment is needed for comparison against the preflight predictions that were used to size the Mach 10 trips. The Mach 10 bluntness increment was previously noted as 0.12-in., which then corresponds to a k/δ of order one being the threshold for when the trips were no longer effective, in qualitative agreement with the simple design philosophy used to size the Mach 10 trips. In other words, based on the local conditions at the trip, when the trip height was appreciably less than the boundary-layer thickness during the Mach 10 flight, the trips were no longer fully effective, which was consistent with the ground-based findings [7].

VII. Conclusions

The successful Mach 7 and 10 Hyper-X flights have provided the opportunity to assess the rationale and methodologies used during the design of the flight vehicles. One decision made early in the design process was to use boundary-layer trips ahead of the inlet to force transition and reduce susceptibility to flow separations in front of and within the scramjet engine. The flight instrumentation layout was selected to provide enough coverage and redundancy to be able to determine and assess the vehicle flight performance. In this case, the surface thermocouple data from the both flights were used to assess the boundary-layer state during each trajectory, both on the lower surface to determine trip effectiveness, and on the upper surface to evaluate the natural transition state of the vehicle. The present paper provides a brief review of the ground-based trip design effort, a presentation of the Mach 7 and 10 flight thermocouple results, an analysis of the temperature-time histories to provide heating rates for determination of the times at which boundary-layer transition occurred, and an assessment of the boundary-layer properties that correspond to those key points along the trajectory. The present analysis has shown for both flights that the lower surface trips performed as expected based on the ground-based program and that the approach taken to scale the trips to flight was acceptable. The upper surface analysis revealed that the preflight hypersonic transition criteria of momentum thickness Reynolds number over the edge Mach number of 300 was a reasonable estimate of transition onset and as such the preflight decision to use trips on the lower surface was warranted.

References

[1] Rausch, V. L., McClinton, C. R., and Crawford, J. L., *Hyper-X: Flight Validation of Hypersonic Airbreathing Technology*, ISABE Paper 97-7024, 1997.

[2] Rausch, V. L., McClinton, C. R., and Hicks, J. W., "NASA Scramjet Flights to Breath New Life into Hypersonics," *Aerospace America*, Vol. 35, No. 7, 1997, pp. 40–46.

[3] McClinton, C. R., Holland, S. D., Rock, K. E., Engelund, W. C., Voland, R. T., Huebner, L. D., and Rogers, R. C., *Hyper-X Wind Tunnel Program*, AIAA Paper 98-0553, 1998.

[4] Ferlemann, S. M., Voland, R. T., Cabell, K., Whitte, D., and Ruf, E., "Hyper-X Mach 7 Scramjet Pretest Predictions and Ground to Flight Comparison," *Presented at 13th International Space Planes and Hypersonic Systems and Technology Conference*, AIAA Paper 2005-3322, May 2005.

[5] Engelund, W. C., and Holland, S. D., "Hyper-X/X-43A Aerodynamics: Results from the Mach 7 and Mach 10 Scramjet Flight Tests," *Presented at 28th JANNAF Airbreathing Propulsion Subcommittee Meeting*, JANNAF, Washington, D.C., 2005.

[6] Voland, R. T. and McClinton, C. R., "NASA Hypersonic Overview," *Presented at 28th JANNAF Airbreathing Propulsion Subcommittee Meeting*, JANNAF, Washington, D.C., 2005.

[7] Berry, S. A., Auslender, A. H., Dilley, A. D., and Calleja, J. F., "Hypersonic Boundary Layer Trip Development for Hyper-X," *Journal of Spacecraft and Rockets*, Vol. 38, No. 6, 2001, pp. 853-864. doi:10.2514/2.3775

[8] Lau, K. Y., "Hypersonic Boundary-Layer Transition: Application to High-Speed Vehicle Design," *Journal of Spacecraft and Rockets*, Vol. 45, No. 2, 2008, pp. 176–183. doi:10.2514/1.31134

[9] Dilley, A. D., "Hyper-X Trip Sizing and Preliminary Drag Estimates," Hyper-X Technical Note 96HN0064, NAS1 19864, 1996.

[10] Stetson, K. F., Thompson, E. R., Donaldson, J. C., and Siler, L. G., *Laminar Boundary Layer Stability Experiments on a Cone at Mach 8,*

Part 2: Blunt Cone, AIAA Paper 84-0006, 1984.
[11] Reshotko, E., "Boundary Layer Stability and Transition," *Annual Review of Fluid Mechanics*, Vol. 8, No. 1, 1976, pp. 311–349. doi:10.1146/annurev.fl.08.010176.001523
[12] Dilley, A. D., "Final Design for Mach 7 Hyper-X Boundary Layer Trips," Hyper-X Technical Note 99-282, NAS1 96013, 1999.
[13] Huebner, L. D., and Rood, R. L., "Instrumentation and Measurement for the Hyper-X Flight Vehicle," *JANNAF CS/PSHS/APS Joint Meetings*, JANNAF, Washington, D.C., Oct. 1997.
[14] Berry, S., Daryabeigi, K., Auslender, A., and Bittner, R., "Boundary Layer Transition on X-43A Flight 2," *JANNAF 28th Airbreathing Propulsion Subcommittee Meeting*, JANNAF, Washington, D.C., June 2005.
[15] Williams, S. D., and Curry, D. M., "Thermal Protection Systems," NASA RP-1289, Dec. 1992.
[16] Chiu, S. A., and Pitts, W. C., *Reusable Surface Insulations for Reentry Spacecraft*, AIAA Paper 1991-0695, Jan. 1991.
[17] Bouslog, S. A., and Cunnington, G. R., Jr., *Emittance Measurements of RCG Coated Shuttle Tiles*, AIAA Paper 1992-0851, Jan. 1992.
[18] Anderson, D. A., Tannehill, J. C., and Pletcher, R. H., *Computational Fluid Mechanics and Heat Transfer*, Hemisphere Publishing, Washington, D.C., 1984.
[19] Throckmorton, D. A., and Hartung, L. C., "Space Shuttle Orbiter Entry Lee-Side Heat-Transfer Data STS-28," NASA RP 1306, Sept. 1993.
[20] Smith, S. A., *Digital Signal Processing, A Practical Guide for Engineers and Scientists*, Elsevier Science, Burlington, MA, 2003.
[21] Daryabeigi, K., Berry, S. A., Horvath, T. J., and Nowak, R. J., *Finite Volume Numerical Methods for Aeroheating Rate Calculations From Infrared Thermographic Data*, AIAA Paper 2003-3634, June 2003.
[22] Engel, C. D., and Praharaj, S. C., "Miniver Upgrade for the AVID System, Vol. I: LANMIN User's Manual," NASA CR-172212, Aug. 1983.
[23] Baranowski, L. C., "Influence of Cross-Flow on Windward Centerline Heating," MDC E0535, Dec. 1971.
[24] Wurster, K. E., and Stone, H. W., "Aerodynamic Heating Environment Definition/Thermal Protection System Selection ofr the HL-20," *Journal of Spacecraft and Rockets*, Vol. 30, No. 5, 1993, pp. 549–557. doi:10.2514/3.25565
[25] Tartabini, P. V., Wurster, K. E., Korte, J. J., and Lepsch, R. A., "Multidisciplinary Analysis of a Lifting Body Launch Vehicle," *Journal of Spacecraft and Rockets*, Vol. 39, No. 5, 2002, pp. 788–795. doi:10.2514/2.3880
[26] Wurster, K. E., Riley, C. J., and Zoby, E. V., "Engineering Aerothermal Analysis for X-34 Thermal Protection System Design," *Journal of Spacecraft and Rockets*, Vol. 36, No. 2, 1999, pp. 216–228. doi:10.2514/2.3452
[27] Zoby, E. V., Thompson, R. A., and Wurster, K. E., *Aeroheating Design Issues for Reusable Launch Vehicles: A Perspective*, AIAA Paper 2004-2535, June 2004.
[28] Eckert, E. R. G., "Survey of Boundary Layer Heat Transfer at High Velocities and High Temperatures," WADC, Tech. Rept. 59-524, April 1960.
[29] Anderson, E. C., and Lewis, C. H., "Laminar or Turbulent Boundary-Layer Flows of Perfect Gases or Reacting Gas Mixtures in Chemical Equilibrium," NASA CR-1893, Oct. 1971.
[30] Johnson, K., *Hyper-X Aerodynamics and Propulsion Reference Systems*, Hyper-X Program Office, HX-241-Rev. A, June 2004.
[31] Bittner, R., "X-43A Second Flight Boundary Layer Analysis Based on the Best Estimated Trajectory Version 2.2 (Rev A)," NASA Langley Research Center, Technical Note 05-453A (NNL07AA00B), Feb. 2008.
[32] Karlgaard, C., "X-43A Flight 2 Best Estimated Trajectory," NASAHX-DFRC-0389, Rev. A, Jan. 2005.
[33] DelCorso, J., "X-43A Flight 3 Data Release (Attachment 3)," NASAHX-1077, May 2005.
[34] Auslender, A., Berry, S., and Dilley, A., "Boundary Layer Trip Selection/Design for the Mach 7 Hyper-X Research Vehicle (HXRV)," Hyper-X Program Office, NASAHX-721, Sept. 1999.

R. Kimmel
Associate Editor